EUROFUSION WP15ER-PR(16) 16596

F Nespoli et al.

Blob properties in full-turbulence simulations of the TCV Scrape-Off Layer

Preprint of Paper to be submitted for publication in
Plasma Physics and Controlled Fusion

This work has been carried out within the framework of the EUROfusion Consortium and has received funding from the Euratom research and training programme 2014-2018 under grant agreement No 633053. The views and opinions expressed herein do not necessarily reflect those of the European Commission.

Blob properties in full-turbulence simulations of the TCV Scrape-Off Layer

F. Nespoli, F. Avino, I. Furno, F.D. Halpern, B. Labit, F. Musil, P. Ricci, F. Riva
Ecole Polytechnique Fédérale de Lausanne (EPFL), Swiss Plasma Center (SPC), CH-1015 Lausanne, Switzerland

Abstract

To investigate blob properties in the tokamak Scrape-Off Layer (SOL) , we perform dedicated numerical nonlinear simulations of plasma turbulence in the SOL of a TCV discharge using the GBS code. A blob detection technique is used for the first time in a full-turbulence simulation to track the motion of the filaments in the SOL. The specific size, density amplitude and radial velocity of the blobs are computed, with the typical values being 7.4 ρ_s, 0.33 n_e and 0.016 c_s, respectively. The analysis of blob structure in the parallel direction shows that the blobs are partially detached from the limiter. The cross correlation analysis shows how the blobs are born all along the entire field line, not being generated primary on the low field side SOL and expanding towards the limiter. The blob radial velocity agrees well with the inertial branch of the existing scaling law. The radial particle and heat fluxes given by blobs are shown to be responsible of up to 100% and 70% of the turbulent particle and heat flux in the far SOL, respectively. The results of a second simulation with a 40 times higher resistivity are also discussed.

1 Introduction

Plasma filaments (blobs) are an ubiquitous feature of plasmas in open magnetic field lines and are routinely detected in the tokamak Scrape-Off Layer (SOL). Due to their radially outwards motion, they are believed to enhance the cross field transport in the SOL [1], contributing substantially to the heat deposition on the first wall and divertor plates, both on the high field side (HFS) and on low field side (LFS). The comprehension of their dynamics is hence of crucial importance for a better prediction of the heat loads onto the first wall. While the blob dynamics has been investigated experimentally in tokamaks [2, 3, 4], basic plasmas experiments [5, 6, 7, 8] and with numerical simulations of single seeded blobs [9, 11, 10], some questions are still open. Indeed, seeded simulations do not give any indication on blob shape and behavior in a SOL plasma. Blob measurements in tokamaks with an exhaustive diagnostic coverage, as done in basic plasmas experiments, is currently prohibitive. Furthermore, the mechanisms governing blob formation and dynamics could differ in basic plasma experiments and in tokamaks SOL.

To have a better understanding of blobs generation and dynamics, we apply for the first time a blob detection technique to a full-turbulence numerical simulation of a plasma discharge. The SOL of a TCV inboard-limited L-mode plasma is modeled using the GBS code. The blobs, generated self-consistently by turbulence, are detected and tracked in time, from their birth to their death.

This paper is structured as follows: in Section 2 we describe the numerical simulations of the TCV SOL using the GBS code [12, 13]. In Section 3, the blob detection and tracking method is described. In Section 4, the birth of the blobs is discussed, while in Section 5, the 3D shape of the blobs is analyzed. In Section 6, the results of the cross-correlation analysis are exposed, confirming the results from the previous section and giving some more insight on blob generation. In Section 7, the velocities resulting from blob tracking are analyzed and compared with an existing scaling law. Finally, in section 8 we quantify the contribution of the blobs to the radial particle and heat fluxes.

2 Nonlinear simulations with the GBS code

We perform dedicated numerical nonlinear simulations using the GBS code [12, 13]. By solving the drift-reduced Braginskii equations, GBS allows for the self-consistent description of equilibrium (time-averaged) and fluctuating quantities in a fully 3D geometry. Effects due to finite aspect ratio, ion temperature and magnetic shear are included in the simulations. The equations determining the plasma dynamics are detailed in Ref. [13, 14]. The boundary conditions at the limiter are described in Ref. [15]. At the inner and outer radial boundaries of the simulations, Neumann boundary conditions are used for all quantities , with the exception of the plasma potential (at the outer boundary) and the vorticity (at both boundaries), for which Dirichlet conditions are imposed. These simulations feature only open field lines and plasma density and temperature sources mimic the injection of plasma from the core into the SOL. The flux surface on which the sources are located corresponds hence to the Last Closed Flux Surface (LCFS) of the real tokamak plasma.
In this paper, the results of two simulations are discussed: in the first one (A), the SOL of a TCV discharge is modeled. It is a circular inboard limited ohmic L-mode deuterium plasma, with plasma current and toroidal magnetic field on axis being $I_p = 145$ kA and $B = 1.45$ T, respectively. The values of the plasma density and temperature at the LCFS, $n_{e0} = 5\times10^{18}$ m^{-3} and $T_{e0} = 25$ eV, are deduced from Langmuir probes embedded in the limiter. They set the normalized Spitzer resistivity $\nu = q_e n_{e0} R_0/(m_i c_{s0}\sigma_\parallel) \propto n_{e0}R_0\Lambda m_e/(m_i c_{s0} T_{e0}^{3/2})$, $\nu = 5.9\times10^{-4}$, and the dimensionless size of the system through the ion sound Larmor radius $\rho_s = m_i c_{s0}/(q_e B) = 0.5$ mm, where Λ is the Coulomb logarithm, $R_0 = 0.84$ m is the major radius of the plasma, c_{s0} is the ion sound speed based on the electron temperature at the LCFS, T_{e0}, and m_i, m_e and q_e are the ion mass, electron mass, and electron charge, respectively. The resulting simulation domain consists of $128\times820\times128$ points in the radial (x), poloidal (y) and toroidal (z) direction, respectively. The sources of plasma temperature and density are located at $x = 20$. The shape of the sources is gaussian in the radial direction with a width of 3 grid points. The sources are poloidally and toroidally uniform.The safety factor $q = 3.2$, the magnetic shear $\hat{s} = 1.5$ and the inverse aspect ratio $\epsilon = 0.24$ are obtained from the magnetic reconstruction of the discharge. The ion temperature at the LCFS is assumed to be $T_{i0} = T_{e0}$, since no ion temperature measurement was available for that discharge. Resistivity can affect substantially blobs dynamics, as predicted in Ref. [16] and experimentally measured in Ref. [3]. To investigate the role of resistivity on blob dynamics, we perform a second simulation (B) identical to the first one, except for the resistivity, which is 40 times larger. The analysis presented in this work is applied to a simulated time interval of 23 R_0/c_{s0} corresponding to 0.55 ms, the results output frequency being 3 MHz. The simulation output result at a given time will be referred to in the following as "frame". The two numerical simulations provide, for every frame, the three-dimensional distribution of the plasma density n (quasi neutrality is assumed), the plasma potential ϕ_p, the electron and ion temperature T_e and T_i, the electron and ion parallel velocities $v_{||,e}$ and $v_{||,i}$. Their time-averaged quantities are described in details in Ref. [17].
A snapshot of the plasma density in a poloidal plane of simulation A is shown in Fig. 1 (left) together with the limiter geometry in the simulation (thick red) and TCV (dashed red) respectively. The set of coordinates that is used in the following is also displayed: θ is the poloidal angle and r_u is the upstream radial coordinate, with $r_u = 0$ at the LCFS. On the right of Fig. 1 a snapshot of the normalized density fluctuation $\delta n/n_0$ is shown. A mode with poloidal number $m = 30$ is visible close to the LCFS. As discussed in Ref. [17], the simulated heat flux profiles agree quantitatively with the experimental ones [18], showing the presence of two distinct regions in the SOL, that can

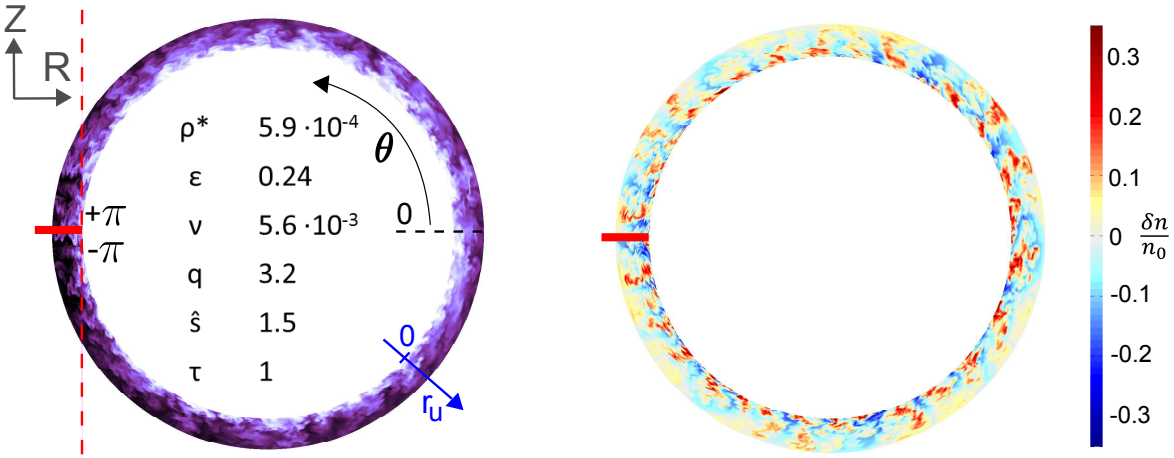

Figure 1: Left: snapshot of plasma density from simulation A. The coordinate system and the simulation (thick red) and TCV (dashed red) limiter geometry are shown. The simulation parameters are displayed: normalized ion sound Larmor radius $\rho^* = \rho_s/R$, inverse aspect ratio ϵ, Spitzer resistivity ν, safety factor q, magnetic shear $\hat{s}$ and ion to electron temperature ratio $\tau = T_{i,0}/T_{e0}$. Right: snapshot of normalized plasma density fluctuation.

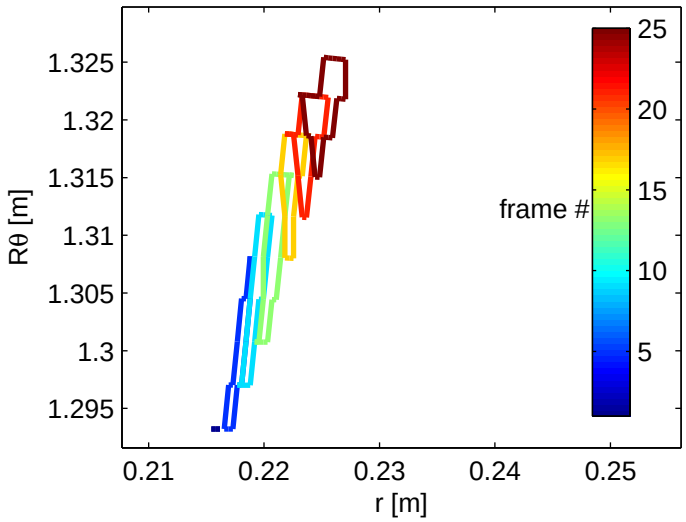

Figure 2: The contour of a blob as detected by the pattern recognition algorithm is plotted in the poloidal plane for subsequent simulation frames.

Simulation	# blobs	merging	splitting	$\langle a_\theta \rangle$	$\langle a_r \rangle$	$\langle a_{\|\|} \rangle$
A ($1 \times \nu$)	5902	23%	24%	7.4 ρ_s	4.5 ρ_s	6026 ρ_s
B ($40 \times \nu$)	7611	22%	30%	6.3 ρ_s	4.3 ρ_s	4460 ρ_s
Simulation	$\langle \delta n_{max}/n_{max} \rangle$	$\langle t_l \rangle$	$\langle \sigma_{l,bottom} \rangle$	$\langle \sigma_{l,top} \rangle$	$\langle v_\theta \rangle$	$\langle v_r \rangle$
A ($1 \times \nu$)	0.33	0.14 R_0/c_{s0}	0.35	0.30	0.011 c_{s0}	0.015 c_{s0}
B ($40 \times \nu$)	0.30	0.16 R_0/c_{s0}	0.16	0.28	0.004 c_{s0}	0.020 c_{s0}

Table 1: Summary of the results from the blob detection method for both simulations. The quantities are defined in the text.

therefore be separated into "near" and "far" SOL. The near SOL, extending a few millimeters from the LCFS, is characterized by steep gradients of plasma temperature and density and is of crucial importance for peak heat loads on the tokamaks first wall. The far SOL, characterized by flatter profiles, is typically a few centimeters wide and is at the origin of the main heat loss channel onto the first wall.

3 Blob detection technique

A pattern recognition technique similar to the one used in [5] on experimental data is used for the first time on full-turbulence simulations to track the motion of the filaments and to study their dynamics. The condition for the blob detection is $n(r_u, \theta, t) > \bar{n}(r_u, \theta) + 2.5\ \sigma(r_u, \theta)$ where $\bar{n}$ and σ are the local toroidally and time-averaged density and its standard deviation, respectively. The different blobs are identified in a given (2D) poloidal plane for every frame of the simulation through pattern recognition. They are then tracked to determine their radial and poloidal velocity v_r, v_θ: two structures on consecutive frames $b_i(t_{k-1})$ and $b_j(t_k)$ are considered to be the same blob if the area A of their intersection is larger than 10% of the area of the structure in the earlier frame: $A(b_i(t_{k-1}) \cap b_j(t_k)) > A(b_i(t_{k-1}))/10$. Blobs living less than 6 frames=$0.08 R_0/c_{s0} = 2\mu$s are discarded from the analysis. The merging of two or more different blobs into a new one or the splitting of one blob into two or more parts are considered as the birth of a new blob. The blob velocity is computed for each frame of its trajectory (except from the first one and the last one for each blob, where it is not defined), as the velocity of the center of mass of the blob.
The blob detection technique is applied to the simulation output, resulting in the detection and tracking of over 5900 blobs for simulation A. A typical result of the blob tracking is shown in Fig. 2, in which the contour of a detected blob is displayed for subsequent frames. The results of the blob detection algorithm are summarized in Table 1. The higher resistivity in simulation B results in the detection of $\sim 30\%$ more filaments, consistently with the increase of the skewness reported in [17]. The blobs originating form merging events account for the 23% (22%) of the total, while 24% (30%) of the blobs results from splitting events, for simulations A (B), respectively. The average life time of the blobs is $\langle t_l \rangle = 0.14 R_0/c_{s0}$ for simulation A and $\langle t_l \rangle = 0.16 R_0/c_{s0}$ for simulation B.

4 Blob generation

In the following we discuss the blob birth spatial distribution resulting from the blob detection algorithm. In Fig. 3(a,b) the histograms of birth events against the radial coordinate are shown for both simulations. From the detection algorithm, the birth of a blob can be due to three different mechanisms: 1) a blob is detected for the first time, i.e. it does not superimpose to any blob present

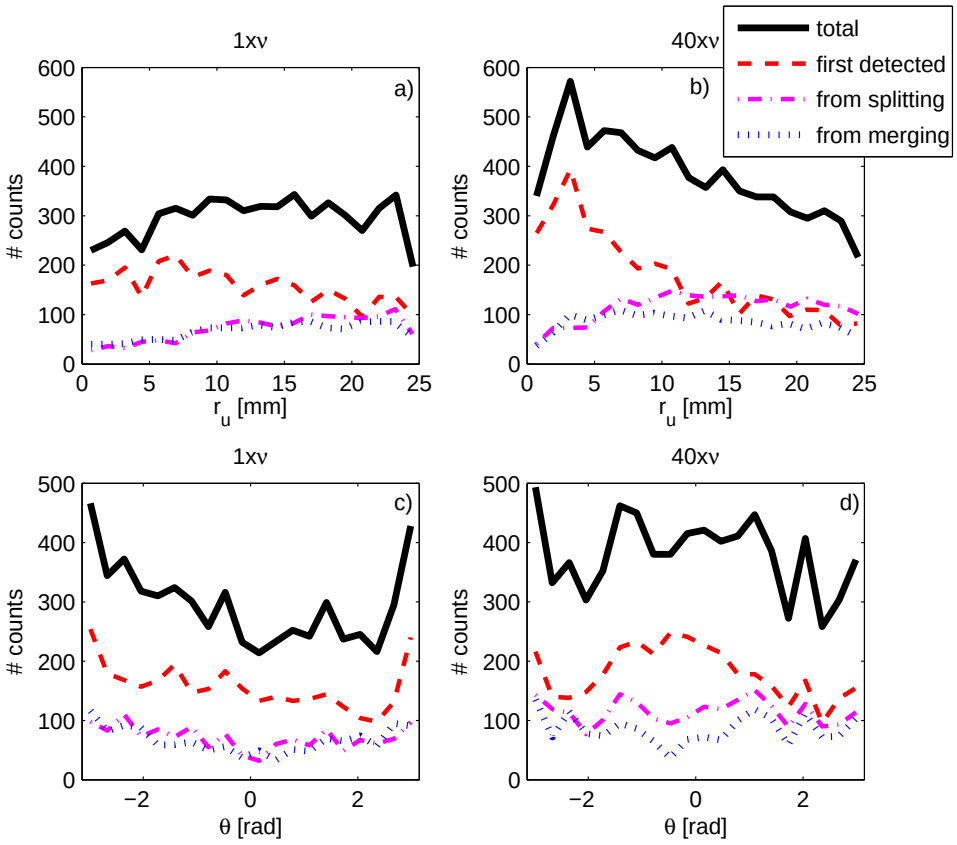

Figure 3: Histograms of the birth events along the radial coordinate r_u (a,b) and along the poloidal coordinate θ (c,d), for simulation A (a,c) and B (b,d). The contribution to the total birth rate (thick black lines) of blobs originating from splitting (dash-dotted magenta) or merging events (dotted blue) is distinguished from the blobs that are detected for the first time (dashed red).

in the previous simulation frame 2) a blob is born from the splitting of a blob in the previous frame into two or more distinct parts 3) a blob is born from the merging of two or more blobs in the previous frame. The histogram of the blob birth position is dominated by the blobs that are detected for the first time (case 1), accounting for $\sim 50\%$ of the total detected blobs for both simulations. The profiles of the birth rate are hence dominated by the "first detected" blobs (red dashed lines in Fig. 3). The radial profile of the blob first detections is quite broad and peaks around $r_u = 6$ mm for simulation A. Increasing the resistivity, the point of maximum birth rate moves radially inwards to $r_u = 3$ mm and the profile is more pronounced. Also, as shown in Fig. 3(c,d), where the histograms of birth events against the poloidal coordinate are shown for both simulations, the blobs are more likely to be first detected at the HFS SOL for simulation A and at the LFS SOL for simulation B. This is consistent with the transport being more ballooned due to at higher resistivity [19].

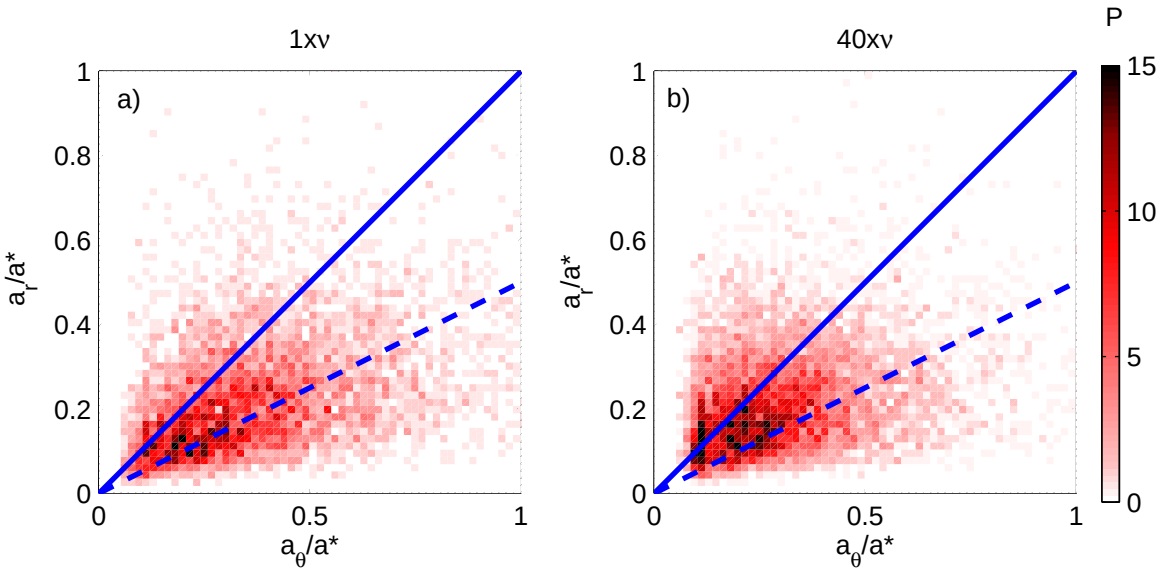

Figure 4: Joint probability distribution P of the poloidal and radial normalized blob size a_θ/a^*, $a_r/a*$ for simulations A (a) and B (b). The lines $a_r = a_\theta$ (solid) and $a_r = a_\theta/2$ (dashed) are plotted to guide the eye.

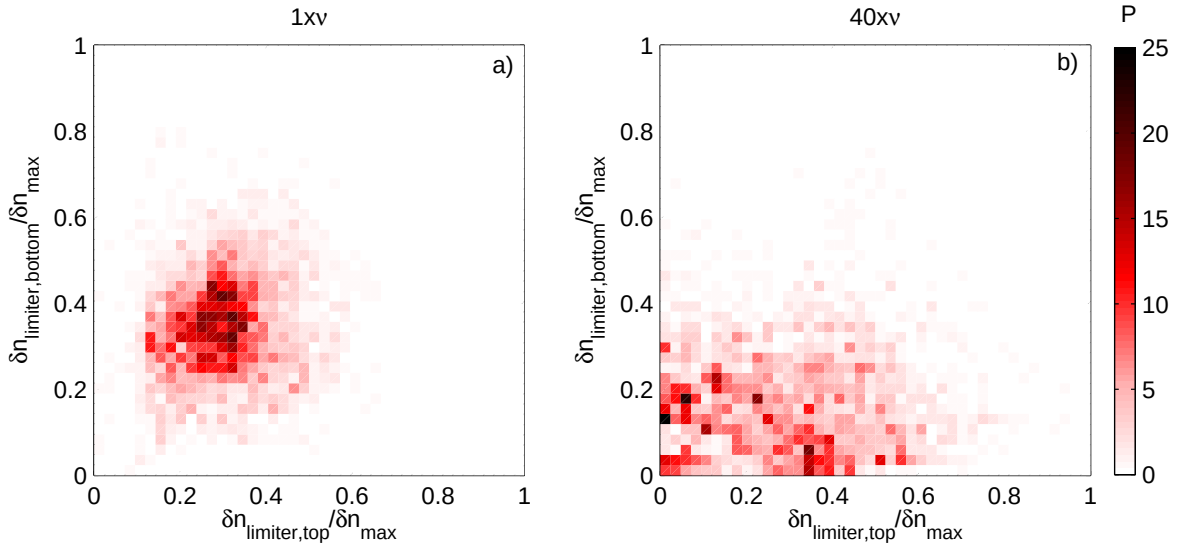

Figure 5: Joint probability distribution P of sheath density drop along the field line $\sigma_l = \delta n_{limiter}/\delta n_{max}$ on the two sides of the limiter. The values of σ_l are displayed for simulations A (a) and B (b) respectively.

5 Characterization of the blob size and shape

Following Ref. [7], we introduce here the typical blob size and velocity:

$$a^* = \left(\frac{4L^2}{\rho_s R}\right)^{1/5} \rho_s, \quad v^* = \left(\frac{2L\rho_s^2}{R^3}\right)^{1/5} c_{s0} \tag{1}$$

where L and R are the connection length and major radius respectively.
The linear size of each blob in the radial and poloidal direction, a_r and a_θ, are computed as the HWHM of the density fluctuation $\delta n(r_u, \theta, t) = n(r_u, \theta, t) - \bar{n}(r_u, \theta)$. The procedure to compute the radial HWHM is described in the following; in the poloidal and parallel direction a similar method is applied. Given a blob b, its density fluctuation at time t is maximum at the point (r_b, θ_b), being $\delta n_{b,max} = \delta n(r_b, \theta_b)$.The radial density fluctuation profile at the blob poloidal location $\delta n(r_u, \theta_b)$ is checked for intersections with the detected areas of all the other blobs in the same simulation frame. The part of the profile not superimposed to any other blob $\delta n'(r_u, \theta_b)$ is extracted. The radial HWHM is then half of the extent of the region for which $\delta n'(r_u, \theta_b) > \delta n_{b,max}/2$. The average poloidal size of the filaments is $\langle a_\theta \rangle = 7.4\rho_s$ and $6.3\rho_s$ for simulations A and B, respectively. This is comparable to the poloidal HWHM of the positive part of the mode shown in Fig. 1, $L_{\theta,HWHM} \sim L_\theta/6 = (2\pi a_{min}/m)/6 = 14\rho_s$. The blobs are found to be elongated in the poloidal direction being $a_r/a_\theta \sim 1/2$, as displayed in Fig. 4, where the joint probability distribution of the poloidal and radial blob size (normalized to the typical blob size a^*) is shown for both simulations. Taking advantage of the 3D geometry of the simulations, the density profile along the field line is extracted for blobs detected in a given 2D poloidal plane. From this profile, the maximum blob (normalized) density fluctuation along the field line $\delta n_{max}/n_{max}$, the blob size in the parallel direction $a_{||}$ and the sheath density drop along the field line $\sigma_l = \delta n_{limiter}/\delta n_{max}$ are determined. Similarly to a_θ and a_r, $a_{||}$ is computed as the HWHM of the fluctuation profile along the field line, $\delta n(r_u, s, t) = n(r_u, s, t) - \bar{n}(r_u, s)$, where s is the coordinate along the field line. The maximum of the density fluctuation along the field line is on average located on the low field side, just above the midplane, the average value of the fluctuation being $\langle \delta n_{max}/n_{max} \rangle = 0.33$ and 0.3 for simulations A and B, respectively. The parallel size is ~ 800 (700) times larger than the poloidal size, corresponding to 35% (26%) of the connection length, for simulation A (B). The average values of the sheath density drop are $\langle \sigma_l \rangle = 0.32$ and 0.22 for simulations A and B, respectively, while the theoretical prediction for the sheath limited case is 0.6 [20]. As shown in Fig.5, where the joint probability of the sheath density drop at the two limiter plates is displayed, the blobs disconnect from the bottom limiter plate for high resistivity (simulation B) while remaining partly attached to the top one. In fact, if we arbitrarily consider a blob detached when $\sigma_l < 0.2$, for simulation B the 66% of the blobs results detached from the bottom plate and the 36% of them are detached from the top one, the average values of the sheath density drop at the two limiter plates being $\langle \sigma_{l,bottom} \rangle = 0.16$ and $\langle \sigma_{l,top} \rangle = 0.28$.

6 Cross correlation analysis

While in the GBS simulations all physical quantities are accessible for the desired time at any point of the 3D domain, experimentally in the tokamak SOL only a number of measurements at fixed locations is available, often with different diagnostics. Typically, fluctuations measurements are carried out at the target (limiter or divertor) using embedded Langmuir probes, while at the LFS one has to rely on gas puff imaging diagnostics [2], reciprocating Langmuir probes [3], or fast framing visible cameras [4]. Cross correlation analysis might be then one of the most powerful and reliable

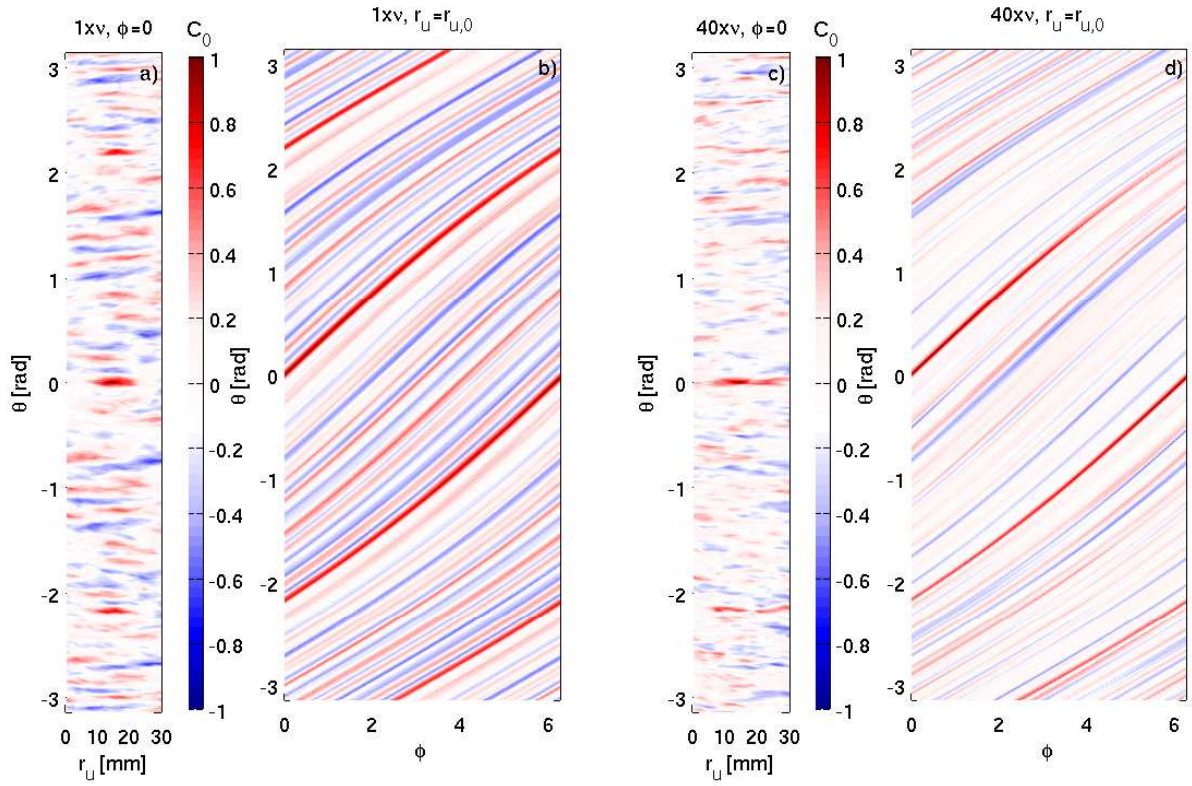

Figure 6: Correlation amplitude at zero time lag C_0 between a point at the outer mid plane ($r_{u,0} = 14\,\mathrm{mm}, \theta = 0, \phi = 0$) and all the other points in the poloidal section defined by $\phi = 0$ (a,c) and on the flux surface $r_u = r_{u,0}$ (b,d), for simulation A (a,b) and B (c,d).

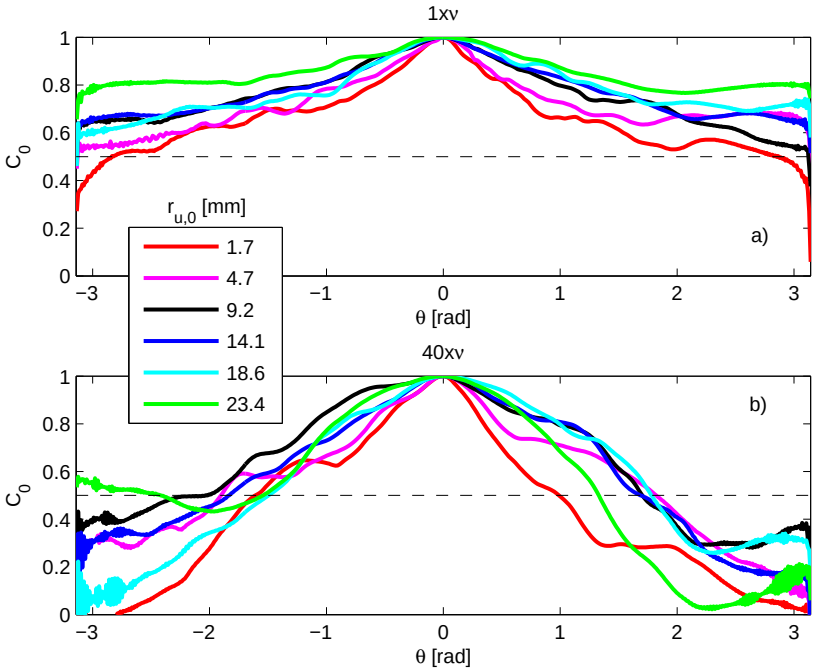

Figure 7: Correlation amplitude at zero time lag C_0 between a point at the outer midplane $(r_{u,0}, \theta = 0, \phi = 0)$ and all the other points along the field line for simulation A (a) and B (b), plotted against the poloidal coordinate θ.

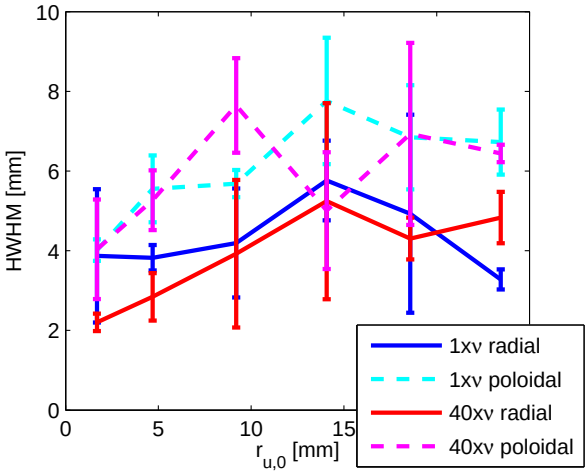

Figure 8: Radial (solid lines) and poloidal (dashed lines) HWHM of the correlation amplitude at zero time lag C_0 between a point at the outer midplane $(r_{u,0}, \theta = 0, \phi = 0)$ and all the other points on the same poloidal plane for simulation A (blue, cyan) and B (red, magenta). The errorbars are given by the difference between the two HWHMs ("left" and "right").

methods to relate target and upstream blob measurements. To give some insight on whether this technique gives valuable results, we perform a cross correlation analysis on the GBS simulations and we compare the results with the ones obtained with the blob detection technique.
We compute the cross correlation between the density time trace at a fixed point at the outer mid-plane ($r_{u,0}, \theta_0 = 0, \phi_0 = 0$) and the density time traces at all the other points in the 3D domain (r_u, θ, ϕ), where ϕ is the toroidal angle. This is done for six different values of $r_{u,0}$ and a typical result is shown in Fig. 6, where the amplitude of the correlation function at zero time lag C_0 is plotted for each point in the poloidal plane and on a flux surface respectively. The correlation clearly peaks along the field line passing through the reference point $(r_{u,0}, 0, 0)$. The profiles of C_0 along the field line are shown in Fig. 7 for simulations A and B, where C_0 is plotted along the field lines for the six reference points at the outer mid plane. The time lag of maximum of correlation τ_{lag}^{max} is always shorter than $7\mu\text{s} \sim 0.04 L/c_{s0}$ along the field line, where L is the connection length. This evidence supports the picture of a blob emerging all along the whole field line from the beginning, rather than being generated mostly on the low field side and progressively elongating towards the limiter.
For simulation A, $C_0 > 0.5$ all along the field line from limiter to limiter, and the correlation increases moving away from the LCFS, as shown in Fig. 7. For simulation B, C_0 drops below 0.5 moving towards the limiters for all the considered $r_{u,0}$ values. The limiter plates and the LFS are therefore decorrelated in simulation B. This picture is consistent with the result of the analysis of the sheath density drop from the 3D structure of the blobs exposed beforehand, showing that blobs disconnect from the limiter as the resistivity increases (Fig. 5). From an experimental point of view, this means that cross correlating measurements performed at the limiter and at the LFS would be possible in the low resistivity case (simulation A) but not in the high resistivity one (simulation B).

In the poloidal cross section (Fig. 6 a,c), the extent of the region for which $C_0 > 0.5$ gives an estimate of the size of the blobs. The variation of the poloidal and radial HWHM of such a region with the radial coordinate $r_{u,0}$ of the reference point used to compute the correlation are displayed in Fig. 8. The blob size estimated in this way varies between 4 and 16 ρ_s, and increases slightly moving radially outwards. These values are compatible with the results from the blob detection algorithm and with what has been found experimentally [2]. Also, the poloidal HWHM is approximately twice the radial HWHM, consistently with the results of the blob detection analysis (Fig. 4).

7 Blob velocity

The detected blob velocities are found to be consistent with the local $\mathbf{E} \times \mathbf{B}$ drift, as shown in Fig. 9, where the blob radial and poloidal velocities resulting from the tracking algorithm v_r, v_θ are plotted against the local components of the $\mathbf{E} \times \mathbf{B}$ drift $v_{E\times B,r}$, $v_{E\times B,\theta}$. The poloidal component of the blob velocity is to be attributed to the background $\mathbf{E} \times \mathbf{B}$ flow, which is mainly poloidal towards the upper limiter. Since the background radial flow is negligible, the blob radial velocity is then consistent with the model [1] of an electrical dipole inside the blob due to vertical charge separation caused by ∇B and magnetic field curvature, resulting in a radial $\mathbf{E}\times\mathbf{B}$ drift. The average blob velocities are $\langle v_r \rangle \cong 0.016\ c_{s0} = 0.15\ v^*$ and $\langle v_\theta \rangle \cong 0.011\ c_{s0} = 0.1\ v^*$ for simulation A. In simulation B the higher resistivity causes the blobs to increase their radial velocity of about 10%, while decreasing their poloidal velocity by approximately a factor 2, being $\langle v_r \rangle \cong 0.02\ c_{s0} = 0.18\ v^*$ and $\langle v_\theta \rangle \cong 0.004\ c_{s0} = 0.036\ v^*$. This is consistent with the substantial decrease in the background $\mathbf{E} \times \mathbf{B}$ flow from simulation A to simulation B, as shown in Ref. [17], and with the disconnection

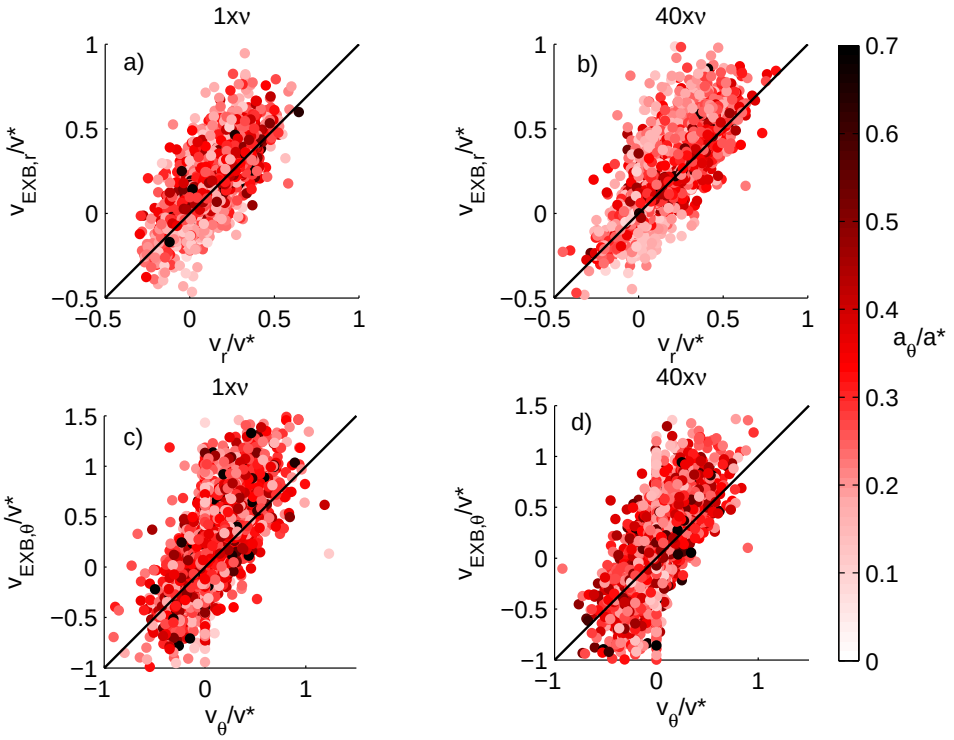

Figure 9: The blob radial and poloidal velocities resulting from the tracking algorithm v_r, v_θ are compared with the local components of the $\mathbf{E} \times \mathbf{B}$ drift $v_{E\times B,r}$, $v_{E\times B,\theta}$, color coded with the blob poloidal size $a_{b,\theta}$. All quantities are normalized according to eq. 1.

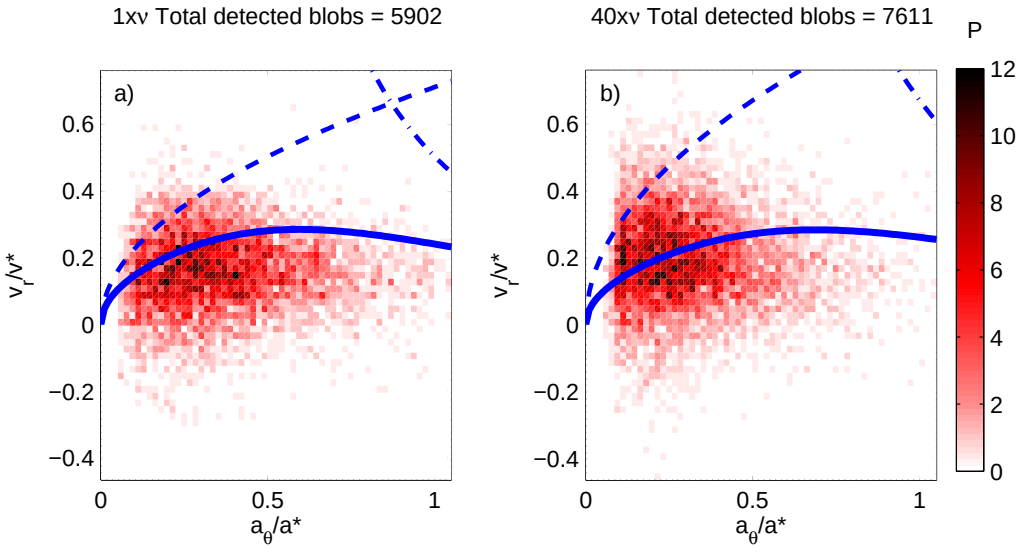

Figure 10: Joint probability distribution P of the normalized blob size in the poloidal plane versus their normalized radial velocity for simulations A (a) and B (b). The scaling in eq. (2) (solid blue lines), its inertial limit $\tilde{v} = \sqrt{\tilde{a}}\dfrac{\delta n/n}{\sqrt{2}\sigma_l}$ (dashed blue lines), and the sheath dominated limit $\tilde{v} = \dfrac{1}{\tilde{a}^2}\dfrac{\delta n/n}{2\sigma_l}$ (dot-dashed blue lines), are also displayed.

of the blobs from the limiter discussed beforehand.
Following Ref. [7], the blob radial velocity and poloidal size are normalized $\tilde{v} = v_r/v^*$ and $\tilde{a} = a_\theta/a^*$, where v^* and a^* are defined in eq. (1). We compare the results of the blob detection analysis with the scaling

$$\tilde{v} = \frac{\sqrt{2\tilde{a}}\ \delta n/n}{1 + 2\sigma_l\sqrt{2}\tilde{a}^{5/2}} \tag{2}$$

from Ref. [7], where the term due to ion-neutral collisions is here neglected, since neutrals dynamics is not included in these simulations. The inertial limit $\tilde{v} = \sqrt{\tilde{a}}\dfrac{\delta n/n}{\sqrt{2}\sigma_l}$ and the sheath dominated limit $\tilde{v} = \dfrac{1}{\tilde{a}^2}\dfrac{\delta n/n}{2\sigma_l}$ can be recovered for $\tilde{a} \ll 1$ and $\tilde{a} \gg 1$, respectively. The comparison is carried out in Fig. 10, where the joint probability distribution of the blob poloidal size versus their radial velocity is plotted for both simulations. The scaling in Eq. (2) is displayed as a continuous blue line, and its inertial and sheath dominated limits are plotted as a dashed and dot-dashed line, respectively. An overall good agreement between the detected velocities and the scaling predictions is found. Furthermore, the agreement is particularly good with the inertial branch of the scaling. This is consistent with the observation of the blobs being partially disconnected at the limiter ($\sigma_l = 0.32$ for simulation A). The agreement with the inertial branch of the scaling is even better for simulation B, where the blobs detach from the bottom plate of the limiter.

8 Blob contribution to particle and heat radial fluxes

Once the blobs are generated, their radial motion is in most cases outwards. We quantify the blob contribution to the radial particle and heat fluxes. In the following, blobs are assumed to have a gaussian profile in the radial and poloidal directions with HWHM a_r, a_θ respectively:

$$\delta n_b(r_u, \theta) = \delta n_{b,max} \exp\left(-\frac{(r_u - r_{u,b})^2}{2\sigma_r}\right) \exp\left(-\frac{[(a_{min} + r_{u,b})(\theta - \theta_b)]^2}{2\sigma_\theta}\right) \tag{3}$$

where $\sigma_r = a_r/\sqrt{\ln 2}$ and $\sigma_\theta = a_\theta/\sqrt{\ln 2}$ are the gaussian widths in the radial and poloidal direction, respectively, $\delta n_{b,max}$ is the maximum of the density fluctuation inside the blob, located at coordinates $(r_{u,b}, \theta_b)$, and $a_{min} = 0.2\,\mathrm{m}$ is the plasma minor radius. The number of particles advected by each blob is computed as

$$\delta N_b = \iint \delta n_b(r_u, \theta)\mathrm{d}r_u\mathrm{d}\theta = \delta n_{b,max} 2\pi\sigma_r\sigma_\theta = \delta n_{b,max}\frac{2\pi}{\ln 2}a_r a_\theta \tag{4}$$

The poloidally and time averaged radial particle flux due to blobs is then computed as

$$\Gamma_b(r_u) = \frac{\sum_b \delta n_{b,max}\dfrac{2\pi}{\ln 2}a_r a_\theta}{2\pi(a_{min} + r_u)\Delta t} \tag{5}$$

where the sum is performed over all the blobs crossing a $r_u = const$ line, and $\Delta t = 0.55$ ms is the simulation time interval used for all the analysis in this paper. This quantity is compared with the turbulent particle flux $\Gamma_t = \langle \delta n \delta v_{E\times B,r} \rangle$ where the brackets mean average over time and poloidal direction. We remark that the turbulent flux is given by blobs and holes. We consider here only the contribution due to positive density fluctuations $\Gamma_{t,+} = \langle \delta n \delta v_{E\times B,r}|_{\delta n>0} \rangle$, resulting in $\Gamma_{t,+} \sim \Gamma_t/2$. We compare Γ_b to $\Gamma_{t,+}$ in Fig. 11a), where the fluxes Γ_t, $\Gamma_{t,+}$ and Γ_b are plotted, for both simulations. The error bars are given by the amount of blobs for which the computation

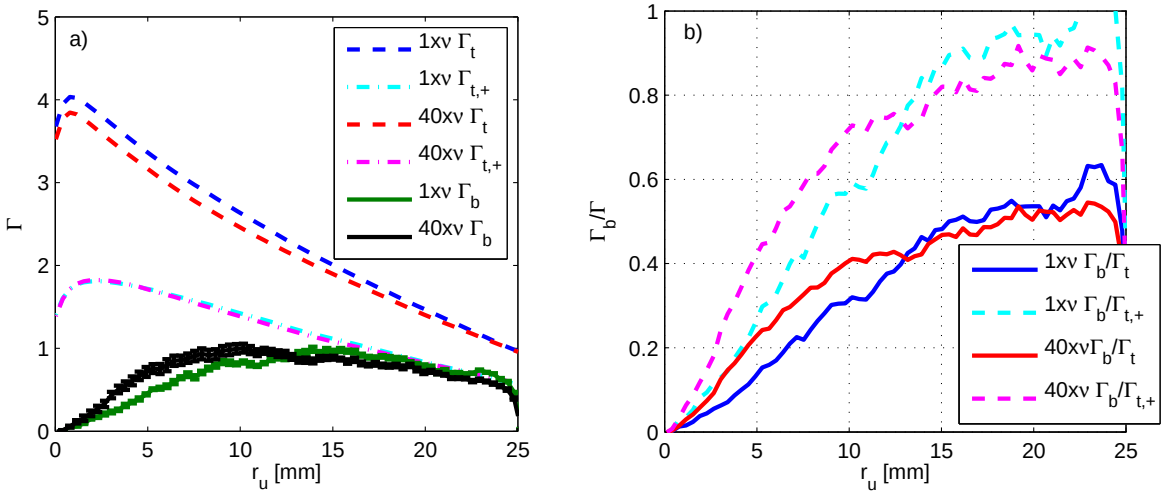

Figure 11: a) particle radial fluxes Γ_b [eq. (5)], Γ_t and $\Gamma_{t,+}$, for both simulations. Errorbars are given by the amount of blobs for which the computation of the HWHMs was not possible. b) ratio of blob particle flux over turbulent particle fluxes.

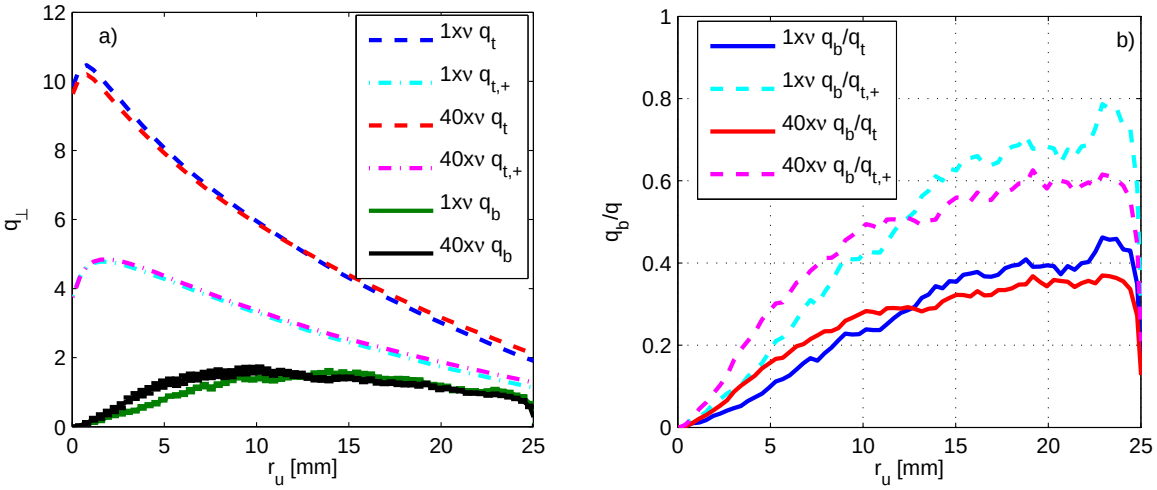

Figure 12: a) heat radial fluxes q_b [eq. (6)], q_t and $q_{t,+}$, for both simulations. Errorbars are given by the amount of blobs for which the computation of the HWHMs was not possible. b) ratio of blob heat flux over turbulent heat fluxes.

of the HWHMs was not possible. As it emerges from Fig. 11b), where the ratios Γ_b/Γ_t and $\Gamma_b/\Gamma_{t,+}$ are displayed, the flux due to blobs contributes only marginally to the turbulent outward flux in the near SOL, while it accounts for up to 100% of $\Gamma_{t,+}$ in the far SOL for simulation A and 90% for simulation B.
We assume that the ion and electron temperature inside a blob are spatially uniform. The poloidally and time averaged radial heat flux due to blobs is then given by

$$q_b(r_u) = \frac{\sum_b \delta n_{b,max} \frac{2\pi}{\ln 2} a_r a_\theta (T_{e,b} + T_{i,b})}{2\pi(a_{min} + r_u)\Delta t} \tag{6}$$

where $T_{i,b}$ and $T_{e,b}$ are computed as the average ion and electron temperature inside the blob, respectively. The shape of the radial profile of the heat flux associated with the blobs $q_b(r_u)$ is qualitatively the same as for the particle flux $\Gamma_b(r_u)$. In Fig. 12 we compare this flux with the turbulent radial heat flux $q_t = \langle \delta p \delta v_{E\times B,r} \rangle$ and with the part of the latter due only to positive pressure fluctuations $q_{t,+} = \langle \delta p \delta v_{E\times B,r} |_{\delta p>0} \rangle$. Similarly to the radial particle flux, we find that the blobs do not contribute substantially to the radial heat flux in the near SOL, while they can contribute up to 70% (60%) of the turbulent flux in the far SOL for simulation A (B), respectively.

9 Conclusions

A blob detection and tracking algorithm is applied for the first time to full-turbulence simulations of the SOL. We consider an inboard-limited plasma in TCV. The blobs are found to be more elongated poloidally than radially and to be partially disconnected from the limiter. The velocities resulting from the blob tracking algorithm are consistent with the local $\mathbf{E}\times\mathbf{B}$ drift, and their radial velocity agrees well with the inertial branch of the scaling presented in Ref. [7]. Once they are generated, the blobs radial motion is mainly outwards. They do not contribute substantially to the particle and heat flux in the near SOL, while they are responsible for up to 100% and 70% of the turbulent particle and heat flux in the main SOL, respectively. Increasing the resistivity by a factor 40 causes the blob to detach from the lower limiter and the point of maximum birth rate moves closer to the LCFS. Also, the blobs are more likely to born at the LFS in the high resistivity case. The correlation analysis confirms the results from the blob tracking algorithm, and shows how the blobs are born already all along the whole field line. The application of the same analysis to ongoing simulations including both open and closed field line regions, whose first results are presented in Refs. [13, 21], is foreseen to better address the physics at the LCFS and in the near SOL, and in particular the blob generation mechanism.

Acknowledgments

The first author gratefully acknowledge useful discussions with N. Fedorczak and O. Chellai. The simulations presented herein were carried out in part using the HELIOS supercomputer system at Computational Simulation Centre of International Fusion Energy Research Centre (IFERC-CSC), Aomori, Japan, under the Broader Approach collaboration between Euratom and Japan, implemented by Fusion for Energy and JAEA; in part in part at the Swiss National Supercomputing Centre (CSCS) under Project ID s549. This work has been carried out within the framework of the EUROfusion Consortium and has received funding from the Euratom research and training programme 2014-2018 under grant agreement No 633053. The views and opinions expressed herein do not necessarily reflect those of the European Commission.

References

[1] S.I. Krasheninnikov, J. Plasma Physics 74 (2008) 679-717

[2] S.J. Zweben, et al., Nucl. Fusion 55 (2015) 093035

[3] D. Carallero, et al., Physical Review Letters 115 (2015) 215002

[4] A. Kirk, et al., Plasma Phys. Control. Fusion 58 (2016) 085008

[5] S.H. Mueller, et al., Phys. Plasmas 13 (2008) 100701

[6] S.H. Mueller, et al., Plasma Phys. Control. Fusion 51 (2009) 055020

[7] C. Theiler, et al., Physical Review Letters 103 (2009) 065001

[8] P. Manz, et al., Physical Review Letters 107 (2011) 195004

[9] D.A. D'Ippolito, et al., Phys. Plasmas 10 (2013) 4029

[10] N. Walkden, et al., submitted to Phys. Plasmas (2016)

[11] F. Riva, et al., Plasma Phys. Control. Fusion 58 (2016) 044005

[12] P. Ricci et al., Plasma Phys. Controlled Fusion 54 (2012) 124047

[13] F. D. Halpern, et al., J. Comput. Phys. 315 (2016) 388-408

[14] A. Mosetto, et al., Phys. of Plasmas 22 (2015) 012308

[15] J. Loizu, et al., Phys. of Plasmas 19 (2012) 122307

[16] J. R. Myra, et al., Phys. Plasmas 13 (2006) 112502

[17] F. Nespoli et al., submitted to Nuclear Materials and Energy (2016)

[18] F. Nespoli, et al., J. Nucl. Mater. 463 (2015) 393-396

[19] A. Mosetto, et al., Phys. of Plasmas 20 (2013) 092308

[20] F.F. Chen and J.P. Chang, Lecture Notes on Principles of Plasma Processing, Kluwer Academic/Plenium Publishers (2003)

[21] F.D. Halpern and P. Ricci, submitted to Phys. of Plasmas (2016)